Pillars of Creation among Destruction: Star Formation in Molecular Clouds near R136 in 30 Doradus

Venu M. Kalari[1] , Mónica Rubio[1], Bruce G. Elmegreen[2] , Viviana V. Guzmán[3], Hans Zinnecker[4,5], and Cinthya N. Herrera[6]

[1] Departamento de Astronomia, Universidad de Chile, Casilla 36-D, Santiago, Chile; venukalari@gmail.com
[2] IBM Research Division, T.J. Watson Research Center, 1101 Kitchawan Road, Yorktown Heights, NY 10598, USA
[3] Joint ALMA Observatory (JAO), Alonso de Cordova 3107 Vitacura, Santiago, Chile
[4] Deutsches SOFIA Institut (DSI), University of Stuttgart, Pfaffenwaldring 29, D-70569, Germany
[5] Universidad Autónoma de Chile, Av. Pedro de Valdivia 425, Santiago, Chile
[6] Institut de Radioastronomie Millimétrique, 300 rue de la Piscine, Domaine Universitaire, F-38406, Saint-Martin-d'Hères, France

Abstract

We present new sensitive CO(2–1) observations of the 30 Doradus region in the Large Magellanic Cloud. We identify a chain of three newly discovered molecular clouds that we name KN1, KN2, and KN3 lying within 2–14 pc in projection from the young massive cluster R136 in 30 Doradus. Excited H_2 2.12 μm emission is spatially coincident with the molecular clouds, but ionized Brγ emission is not. We interpret these observations as the tails of pillar-like structures whose ionized heads are pointing toward R136. Based on infrared photometry, we identify a new generation of stars forming within this structure.

1. Introduction

30 Doradus is a giant H II region in the Large Magellanic Cloud (LMC). The LMC is a dwarf galaxy in the Local Group that lies at a distance of 50 kpc (Pietrzyński et al. 2013) and has a mean stellar metallicity (Z) half that of the Sun (Rolleston et al. 2002). 30 Doradus hosts the young massive cluster (YMC) R136. R136 is a ~1.5–3 Myr YMC that encloses a total cluster mass in excess of $10^5\,M_\odot$ within 10 pc (Selman & Melnick 2013). The cluster contains roughly 200 massive stars ($>8\,M_\odot$) within a central region of less than 6 pc, whose radiation and mechanical feedback profoundly impact the surrounding medium (Schneider et al. 2018). R136 is the most massive YMC in our local neighborhood that can be adequately resolved spatially (at 50 kpc, the nominal distance to R136, $1'' \approx 0.25$ pc), enabling us observe individual objects at the scale of stars and molecular clumps. This makes R136 an ideal laboratory in which to examine how feedback from massive stars affects further star formation (e.g., Dale et al. 2012).

The mechanical and radiative output from R136 has created a central cavity by sweeping the surrounding molecular clouds (labelled as clouds 6 and 10 in Figure 1) that extend up to 100 pc along the northeast–southwest axis (Pellegrini et al. 2010). We adopt the cloud nomenclature of Johansson et al. (1998). Brightly illuminated arcs delineate the interfaces between the cold gas and the ionizing radiation, where subsequent generations of stars are thought to have been triggered (Walborn et al. 2002). Studies at optical (De Marchi et al. 2011; Kalari et al. 2014), near-infrared (nIR; Rubio et al. 1998; Brandner et al. 2001), mid-infrared (mIR; Whitney et al. 2008; Gruendl & Chu 2009; Walborn et al. 2013), far-infrared (fIR; Seale et al. 2014), and submillimeter (Johansson et al. 1998; Indebetouw et al. 2013) wavelengths have identified evidence for active star formation throughout the 30 Doradus nebula, consistent with the idea of multiple episodes of star formation.

We focus on the "stapler nebula," which lies 2–14 pc away from R136 (see Figure 1) in projection. The stapler nebula is the H II region including and surrounding the stapler-shaped

dark cloud that is seen in silhouette in the optical near R136. The nebula spans an area of $1'.1 \times 0'.35$ centered on $\alpha = 05^{\rm h}38^{\rm m}40^{\rm s}$, $\delta = -69°05'36''$ and is elongated with a position angle of 35°. A candidate young stellar object (YSO) has been reported at the edge of the elongated dark cloud by Walborn et al. (2013, marked as S5 in that paper). The YSO is close to, but not coincident with, a region of high density ($n > 10^6\,{\rm cm}^{-3}$) reported by Rubio et al. (2009) using CS line observations. Objects with known infrared excess, some of which are thought to be disk/envelope-bearing YSOs, are dotted toward the edge of the dark cloud according to Rubio et al. (1998; their Figure 3). The literature evidence for dense molecular gas and YSOs in the stapler nebula lying near R136 indicates that star formation may be on-going, which deserves further study. In this paper we discuss the properties of molecular clouds in the stapler nebula, and examine whether new stars are being formed in these clouds.

This paper is organised as follows. In Section 2 we describe the data used in this study. The results from the analysis of CO (2–1) line observations are presented in Section 3. We discuss the results obtained from nIR emission line images of the stapler nebula in Section 4. Based on archival infrared photometry, we identify YSOs within the stapler nebula in Section 5. The picture obtained from our results is described in Section 6. In Section 7, a brief summary of our paper is presented along with future work arising from our results.

2. Data

2.1. CO(2–1) Observations

We conducted a deep CO(2–1) survey centered on the 30 Doradus nebula using the Swedish–ESO submillimeter telescope (SEST) from 1997 March to 2001 January. SEST was a 15 m radio telescope located at La Silla, Chile. The angular resolution at the CO(2–1) frequency of 230 GHz is 23″, which corresponds to a projected size of 5.6 pc at the distance to the LMC.
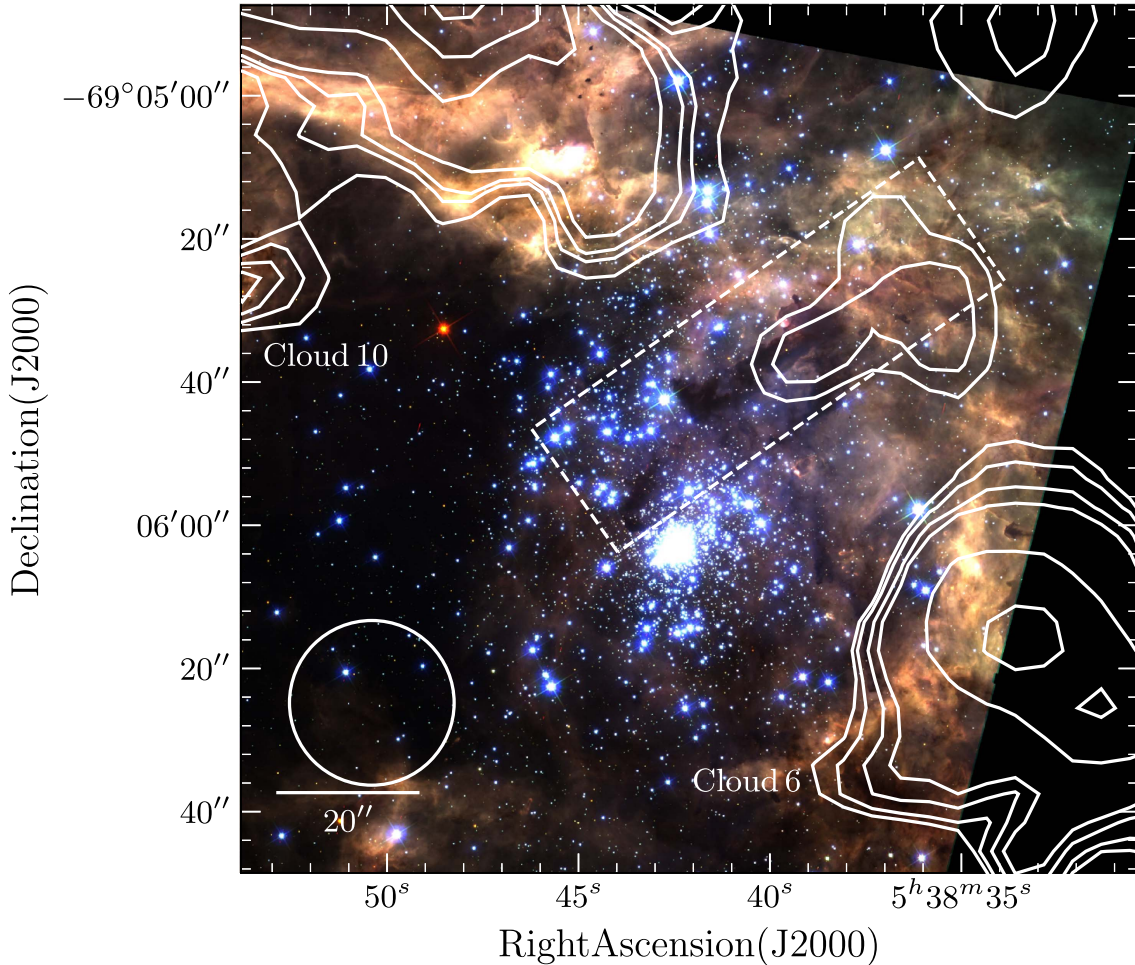
Figure 1. $B/V/I$ Hα (=b/g/r) three-color *HST* image of 30 Doradus, spanning $2' \times 2'$, centered near R136. North is up and east is to the left, with the scale bar at the lower left indicating $20''$. At the distance to the LMC, $20'' \approx 5$ pc. R136 is visible as the bright star cluster at $\alpha = 05^h42^m$ and $\delta = -69°06'$. The white dashed rectangle marks the boundary of the stapler nebula discussed in this work. CO(2–1) contours are shown in white, with the beam size given by the lower left circle. The emission is integrated over the velocity range of 235–270 km s^{-1}. Contour levels are from 0.8 to 2.4 K km s^{-1} in steps of 0.4 K km s^{-1} and from 3.2 to 10 K km s^{-1} in steps of 0.8 K km s^{-1}.

Observations were conducted in position switching mode using a reference point free of CO(2–1) (at $\alpha = 05^h37^m54^s$, $\delta = -69°04'24''$) for sky subtraction. The backend narrow-band high-resolution spectrometer (HRS) was used with a bandwidth of 80 MHz, and a frequency resolution of 41.7 kHz, which translates to a velocity resolution of 0.054 km s^{-1} at the frequency of CO(2–1). The data were reduced using the GILDAS software,[7] with a linear or third-order polynomial for baseline fitting. The resultant spectra were smoothed to a velocity resolution of 0.25 km s^{-1}. The rms noise achieved in a single channel is 0.07 K after 240 s of integration. We mapped the 30 Doradus region with $10''$ spacings and detected CO(2–1) emission across 30 Doradus, including the stapler nebula where CO(1–0) emission had not previously been detected (Johansson et al. 1998; Pineda et al. 2009). In Figure 1, the CO(2–1) contours are overlaid on a three-color optical BVIHα image of 30 Doradus from the *Hubble Space Telescope* (*HST*), where the position of CO(2–1) emission with respect to the R136 cluster can be visualized together with its ionized surroundings. Our observations represent a fivefold increase in sensitivity at twice the spatial resolution of previous CO(1–0) observations across

the 30 Doradus nebula (see Pineda et al. 2009). Observations of the 30 Doradus nebula with higher angular resolution are presented in Indebetouw et al. (2013), Anderson et al. (2014), and Nayak et al. (2016), but those data do not cover the region studied here.

2.2. Near-infrared Emission Line Imaging

We obtained nIR imaging of the 30 Doradus region in the H$_2$ 2.12 μm narrowband filter and the Ks broadband filter using the ISAAC (Infrared Spectrometer and Array Camera) imager mounted on the 8 m Melipal (UT3) telescope of the Very Large Telescope (VLT) situated in Paranal, Chile (program ID 078.C-0487A). Toward the R136 region, the mosaic covered a field of area $5' \times 5'$. The average seeing measured from the images is $\sim 0.''8$–$1.''1$. Observations were taken in the ABBA sequence with the sky image $30'$ from the stapler nebula at $\alpha = 05^h39^m01^s$, $\delta = -69°42'36''$ in a region free of nebulosity within the ISAAC field of view, ensuring adequate sky subtraction. The total integration time on source was 1 hour for the narrowband filter and 100 s for the Ks broadband filter. Data were reduced using the ISAAC pipelines, with flux calibration carried out using the standards of Persson et al.
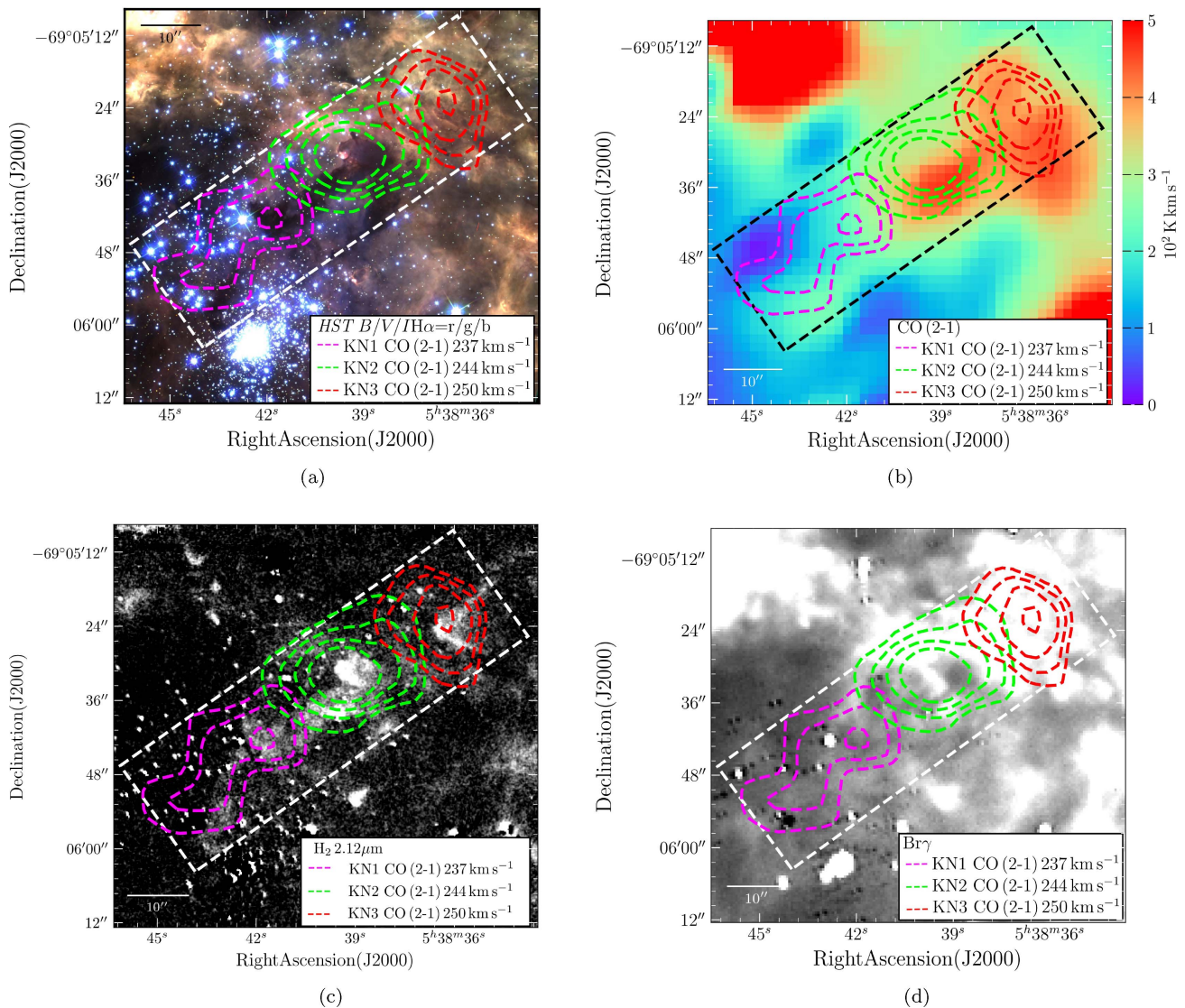
Figure 2. (a) The stapler nebula enlarged from the *HST* mosaic in Figure 1. The stapler region is outlined with the dashed white box. The CO(2–1) contours integrated over 235–240 km s^{-1}, 240–245 km s^{-1}, and 245–250 km s^{-1} are shown in magenta, green, and red respectively and given in the bottom right corner, with the peak velocities of each cloud. The scale bar marks 10″ (at the distance to 30 Doradus, 10″ ≈ 2.5 pc). (b) The total integrated CO(2–1) emission over entire velocity range with the color scale giving the intensity of the emission in 10^2 K km s^{-1}. The CO contours from Figure 2(a) are shown, and the region delineating the stapler nebula is marked by the black dashed lines. (c) Grayscale VLT-ISAAC image of H$_2$ 2.12 μm emission showing the excited molecular gas in the stapler nebula. Scale is logarithmic. The corresponding cold molecular gas from Figure 2(a) and the boundary of the stapler region are shown. The clumpy H$_2$ emission coincides spatially with the center of each CO cloud knot. (d) Grayscale Brγ emission, with the contours from Figure 2(a) and the boundary of the stapler nebula overlaid. Stretch is on a linear scale. In contrast to the H$_2$ emission, the Brγ emission shows no strong spatial coincidence with the centers, but rather with the weakest CO(2–1) contours. A description of the data presented in the figure is found in Section 2, with a discussion in Section 4.

(1998). Astrometric calibration was refined using 2MASS (Two Micron All Sky Survey; Cutri et al. 2003). Bright stars are saturated in the emission line images and have a nonlinear CCD response, meaning they cannot be completely subtracted. This leads to circular bright residuals (and in some cases vertical bleeding) in the emission line images. We excluded these regions from further analysis by masking them.

We used the Brγ 2.165 μm narrowband flux-calibrated image from Yeh et al. (2015). The image was obtained using the NOAO Extremely Wide Field Infrared Imager (NEWFIRM) mounted on the 4 m Victor Blanco telescope located at the Cerro Tololo Inter-American Observatory, Chile. The final Gaussian convolved image resolution for the Brγ narrowband image is 1″, and is comparable to that for the VLT H$_2$ 2.12 μm narrowband image.

2.3. Archival Photometry

mIR photometry of point sources in the stapler nebula was estimated by Gruendl & Chu (2009) from images at 3.6, 4.5, 5.8, and 8.0 μm taken using the *Spitzer Space Telescope* IRAC (Infrared Array Camera) as part of the *Spitzer* legacy program SAGE (*Spitzer* Survey of the Large Magellanic Cloud: Surveying the Agents of a Galaxy's Evolution; Meixner et al. 2006). The FWHM of the images is 1″6, 1″7, 1″7, and 2″ respectively. Alternative photometry of point sources from the same images is also presented by Whitney et al. (2008), but those authors miss a significant fraction of point sources in the 30 Doradus region, because their study is motivated toward detecting reliable sources throughout the LMC via pipeline analysis. Gruendl & Chu (2009) detect objects in the dense and nebulous surroundings using detailed aperture photometry (see

Section 6.3 of Gruendl & Chu (2009) for a comparison). Photometry in the fIR at 100 and 160 μm, and at 250 and 350 μm, of point-like and extended sources in the stapler nebula is given in Seale et al. (2014) using images taken by the *Herschel Space Telescope* instruments PACS (Photoconductor Array Camera and Spectrometer) and SPIRE (Spectral and Photometric Imaging Receiver) respectively as part of the *Hershel* large program HERITAGE (HERschel Inventory of The Agents of Galaxy Evolution; Meixner et al. 2013). The FWHM for these images is 8″, 12″, 18″, and 25″ respectively. We utilize the photometry from Gruendl & Chu (2009) and Seale et al. (2014) in this study.

3. Molecular Clouds

Figure 1 shows the CO(2–1) integrated line emission over the velocity interval 235–270 km s^{-1} as contours, superimposed on the *HST* composite *BVI*Hα image. Strong CO (2–1) emission from Cloud 10 (northeast region of the map) and Cloud 6 (southwest region of the map) previously reported by Johansson et al. (1998) is seen along the northeast–southwest axis.

We observe previously undetected CO(2–1) emission originating from the region located between Clouds 6 and 10, close to R136 (see Figure 2). The emission extends along the southeast–northwest direction in projection. The distance of the emission from R136 in projection is between 2 pc (emission is located to the north of R136) and 14 pc away (in the northwest direction from R136). This CO emission is approximately five times weaker than the CO emission observed in Clouds 6 and 10. This emission is coincident spatially with the stapler nebula in the optical image of Figure 2(a). The emission is resolved in CO(2–1) velocity as a chain of small and weak clouds (Figures 2(a), (b)). We define the stapler region by the extent of the CO(2–1) emission, which goes beyond the visible stapler-shaped dark cloud in the optical. This boundary is marked in Figure 1 with a dashed rectangle. We named the CO clouds Knots (KN), because they form a chain separated in velocity, as demonstrated by the position–velocity slice across the stapler nebula and the CO(2–1) spectra of each individual cloud shown in Figure 3. By analysing the radial velocities and spatial distribution we found that the KN clouds are composed of three clouds we name KN1, KN2, and KN3 in order of decreasing R.A. (labelled in Figure 2(a)).

3.1. Physical Properties

After identifying each cloud, we computed the central velocity (V_{lsr}) in the frame of the local standard of rest and the velocity width (σ_v) by fitting a Gaussian profile to the total cloud spectrum. The sizes of the major and minor axes of the profiles in conjunction with the rms size of the beam were used to compute the deconvolved radius (r). Given that the uncertainties on the Gaussian fit of the CO spectra found for each cloud are around 30%, we estimate the uncertainties on r to be 15%.

3.1.1. CO Luminosity and Mass

The CO cloud luminosity is computed as

$$L_{\mathrm{CO}} \,[\mathrm{K\ km\ s^{-1}\ pc^{-2}}] = D^2 \int_{\Omega} \int_{\nu} T_{\mathrm{mb}}(\nu)\, d\nu\, d\Omega \qquad (1)$$


(a)

(b)

(c)
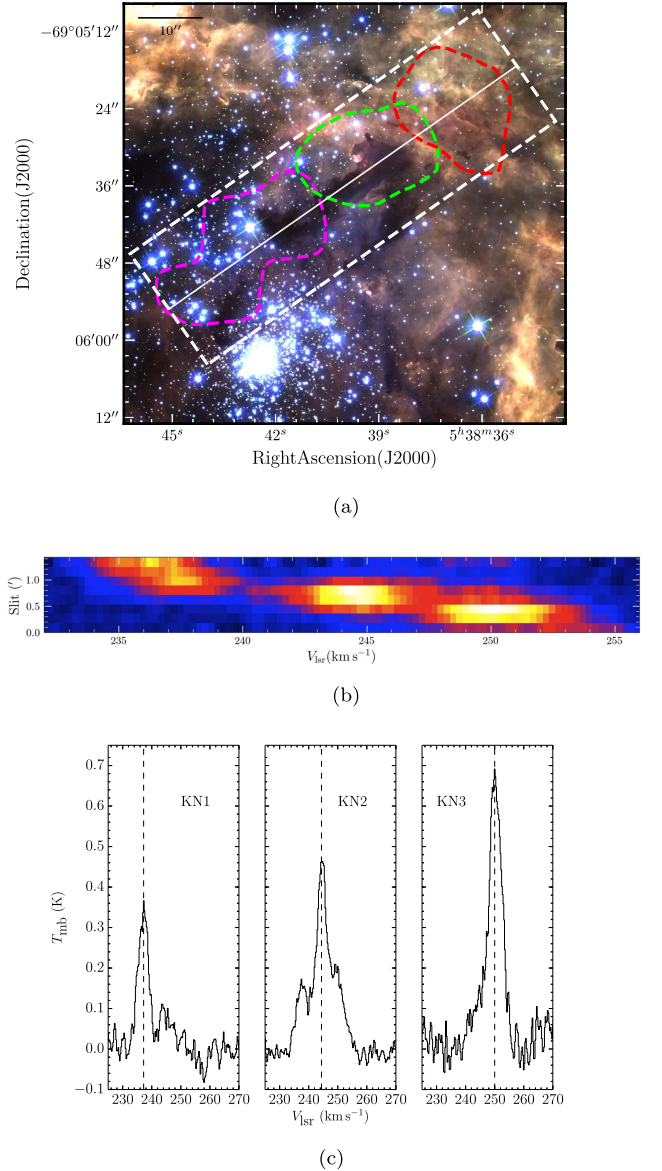
Figure 3. (a) The stapler nebula enlarged from the *HST* mosaic in Figure 1, with the stapler region outlined with the dashed white box. The outermost CO (2–1) contours integrated over 235–240 km s^{-1} and 245–250 km s^{-1} are shown in magenta and red respectively, with the second outermost contour of 240–245 km s^{-1} also shown. The solid white line marks the position of the slice shown in (b). (b) Position–velocity slice of the CO(2–1) cube on a linear scale along the direction of the slit given by the solid white line in (a). The slit cuts along the center of the stapler nebula. (c) CO(2–1) spectra of each cloud extracted from the region bounded by the contours shown in (a). The dashed line for each cloud is its V_{lsr} given in Table 1.

where D is the distance to the source in pc (adopted as 50 kpc), T_{mb} the main beam temperature, which is the antenna temperature corrected for the efficiency of the antenna ($T_{\mathrm{mb}} = T_{\mathrm{A}}/\eta$), and Ω is the solid angle subtended by the source.

The H$_2$ mass of the clouds can be calculated from the observed CO(1–0) luminosity assuming a linear conversion between the velocity-integrated CO emission (I_{CO}) and the H$_2$ column density ($N_{\mathrm{H_2}}$):

$$N_{\mathrm{H_2}} = X_{\mathrm{CO}} \,[\mathrm{cm^{-2}(K\ km\ s^{-1})^{-1}}]\, I_{\mathrm{CO}} \,[\mathrm{K\ km\ s^{-1}}], \qquad (2)$$
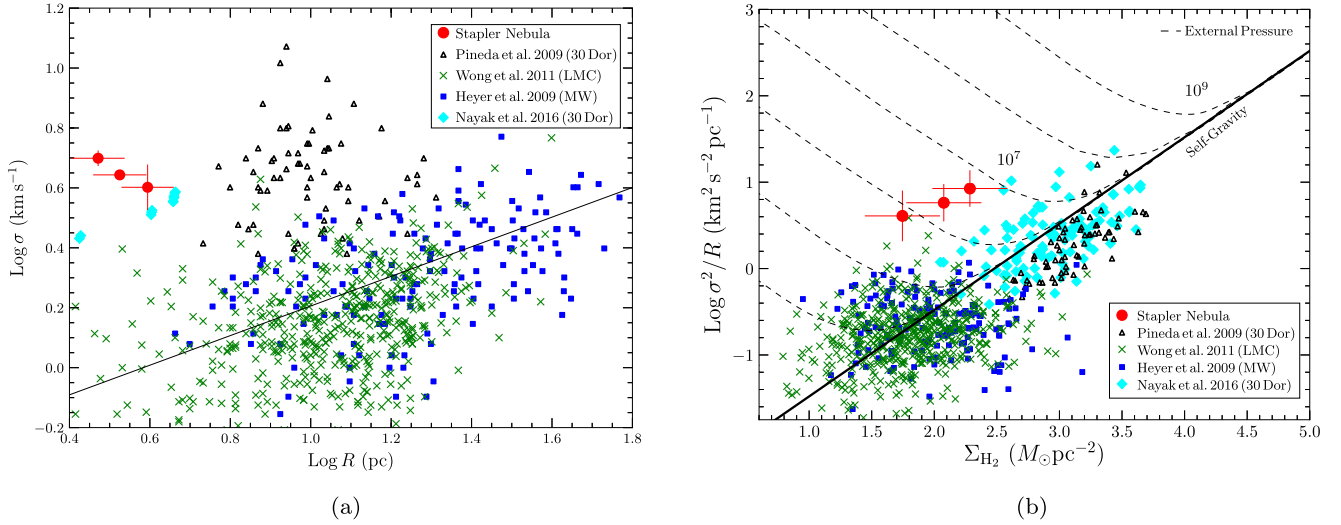
Figure 4. (a) Relation between line width and size for CO(2–1) clouds identified near R136 (circles). The positions of clouds in the 30 Doradus region from Pineda et al. (2009) are shown as triangles, and green crosses mark clouds identified in the LMC by Wong et al. (2011). Cyan diamonds are data in 30 Doradus from Nayak et al. (2016). Blue squares are Galactic molecular clouds from Heyer et al. (2009), which follow the canonical relation of $\sigma_v = 0.72\,R^{0.5}$. (b) The $\sigma_v^2/r - \Sigma_{H_2}$ relation of the stapler molecular clouds, plotted alongside results from the literature (symbols as in part (a)). The solid line gives the approximate σ_v^2/r value for increasing Σ_{H_2} of an isolated virialized cloud confined by self-gravity. The dashed lines mark the equilibria for external pressures $P/k_B \sim 10^3$ to 10^9 cm^{-3} K of a centrally concentrated cloud approximated by hydrostatic equilibrium. The LMC clouds (including those in 30 Doradus) and Galactic molecular clouds appear confined by self-gravity, whereas the KN clouds require pressures $\gtrsim 10^6$ cm^{-3} K to confine them. The large line widths therefore reflect the fact that the clouds are likely confined by external pressure.

Table 1
Properties of the Molecular Clouds

Name	R.A. (J2000)	Decl. (J2000)	V_{lsr} (km s^{-1})	σ_v (km s^{-1})	L_{CO} (K km s^{-1} pc^2)	r (pc)	M_{H_2} ($10^3\,M_\odot$)	M_{vir} ($10^3\,M_\odot$)
30 Dor-KN1	$5^h38^m45^s$	$-69°06'00''$	237.2 ± 0.1	4.0 ± 0.7	154.2 ± 21.3	3.93 ± 0.58	2.7 ± 0.2	10.9 ± 3.3
30 Dor-KN2	$5^h38^m40^s$	$-69°05'30''$	244.4 ± 0.2	4.4 ± 0.1	243.6 ± 3.7	3.35 ± 0.5	4.2 ± 0.3	11.25 ± 1.8
30 Dor-KN3	$5^h38^m36^s$	$-69°05'30''$	250.0 ± 0.2	5.0 ± 0.3	320.8 ± 44.3	2.96 ± 0.44	5.3 ± 0.4	12.83 ± 2.5

where X_{CO} is the CO-to-H$_2$ conversion factor (Bolatto et al. 2013; Roman-Duval et al. 2014). The total mass of H$_2$ (M_{H_2}) is

$$M_{H_2}\,[M_\odot] = \alpha_{CO}D^2\,[\text{Mpc}]S_{CO}, \qquad (3)$$

where

$$\alpha_{CO}\,[M_\odot\,\text{Mpc}^{-2}(\text{Jy km s}^{-1})^{-1}] = X_{CO}\frac{m_{H_2}c^2}{2k\nu^2}, \qquad (4)$$

and the flux density S_{CO} is

$$S_{CO}\,[\text{Jy km s}^{-1}] = \int S_\nu\,dv. \qquad (5)$$

The mass of molecular gas is multiplied by 1.36 to include the helium contribution. This method is calibrated for the $J = 1 \rightarrow 0$ transition. We use a ratio between the CO $J = 2 \rightarrow 1$ and $J = 1 \rightarrow 0$ lines of 0.87 for Cloud 10 of 30 Doradus (the northeastern cloud; see Figure 1) found by Johansson et al. (1998) to estimate the CO(1–0) luminosity.

The conversion factor depends on both metallicity and the intensity of the ambient radiation field (Maloney 1988). As a consequence of strong radiation fields and poor self-shielding in low-metallicity environments, the CO molecule is photo-dissociated because it does not self-shield like the H$_2$ molecule. Therefore, the abundance of CO compared to H$_2$ is less in the Magellanic Clouds than in the Galaxy. This translates into higher values of X_{CO} in the LMC than in the Galaxy. In general

the conversion factor increases with higher radiation fields and decreases with higher metallicities. We adopt the median conversion factor in the LMC compiled from the literature by Bolatto et al. (2013) of

$$X_{CO} = (8.8 \pm 0.3) \times 10^{20}\,[\text{cm}^{-2}(\text{K km s}^{-1})^{-1}]. \qquad (6)$$

The adopted X_{CO} factor is 3.8 times larger than the canonical Galactic X_{CO} of Bolatto et al. (2013). Our adopted value is similar to that found by Herrera et al. (2013) when comparing estimates of molecular and dust mass in the LMC N11 region, but higher than the value of 6×10^{20} cm^{-2} (K km s^{-1})$^{-1}$ reported by Roman-Duval et al. (2014). The resulting cloud masses if we adopted the X_{CO} of Roman-Duval et al. (2014) would be reduced by ~20%.

3.1.2. Virial Mass

The virial mass (M_{vir}) was computed assuming that each cloud is spherical, is in virial equilibrium, and has a density (ρ) profile of the form $\rho \propto r^{-1}$. The virial mass is given by

$$M_{vir}\,[M_\odot] = 190\sigma_v^2\,[\text{km s}^{-1}]\,r\,[\text{pc}] \qquad (7)$$

according to MacLaren et al. (1988). The results of our analysis for each cloud are given in Table 1.
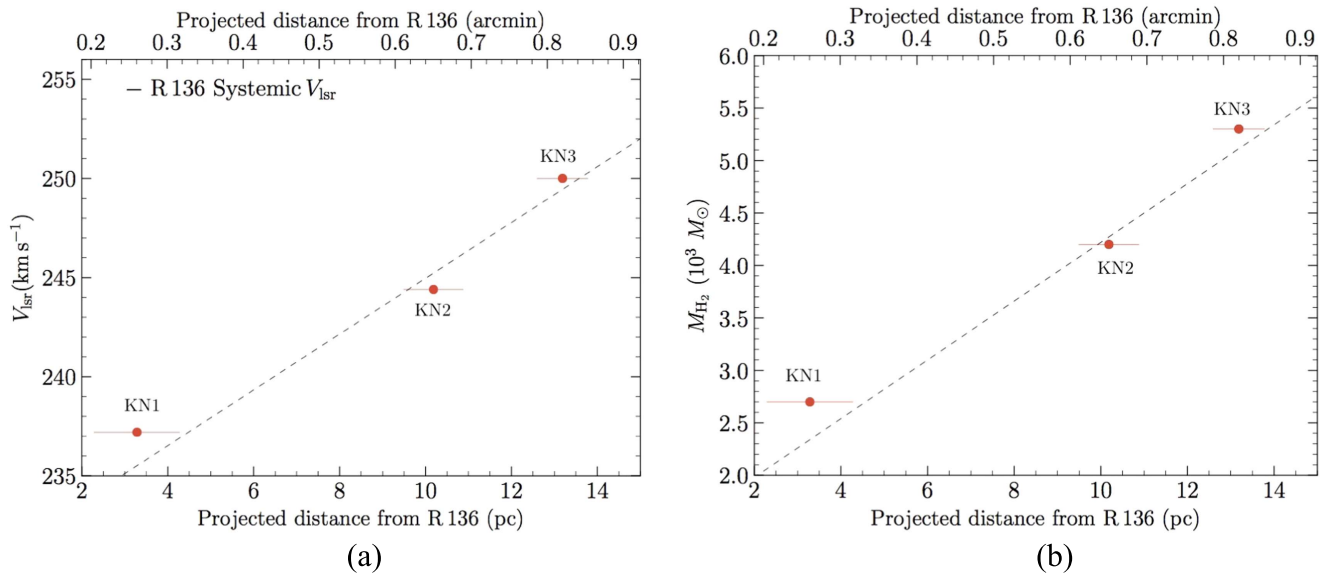
Figure 5. (a) The peak velocity in the frame of the local standard of rest (V_{lsr}) of each cloud is plotted as a function of projected distance from R136. The upper y-axis gives the projected distance in arcmin, while the lower y-axis gives it in parsecs assuming a distance of 50 kpc. The best-fit relation is given by the dashed line and has a slope of $\sim$1.5. (b) The mass of each cloud M_{H_2} is plotted as a function of projected distance from R136. The upper y-axis gives the projected distance in arcmin, while the lower y-axis gives it in parsecs assuming a distance of 50 kpc. The best-fit relation is given by the dashed line.

3.2. Analysis

3.2.1. Larson's Laws

Molecular clouds in virial equilibrium follow the empirical power-law relation $\sigma_v \propto r^\alpha$ (Larson 1981). α is generally agreed to be 0.4–0.5 based on numerous molecular cloud surveys of the Milky Way, and external normal and dwarf galaxies (Bolatto et al. 2008; Heyer et al. 2009). The observed value of α is often explained by turbulence (McKee & Ostriker 2007; Lombardi et al. 2010). The velocity dispersion is considered to be a measure of the internal dynamics within the clouds, because the observed line profiles, averaged over a cloud, have Gaussian shapes and their line widths are broader than the thermal line widths. It is a reasonable assumption to make that the line profiles are produced by turbulent motions of the gas inside the clouds (Solomon et al. 1987).

Figure 4(a) displays the position of the KN clouds in the σ_v–r diagram. Also shown are results from Heyer et al. (2009) summarizing the canonical relation found for Galactic clouds of $\sigma_v = 0.72\ r^{0.5}$, results for clouds in the 30 Doradus region (from Pineda et al. 2009 having a resolution of 43″, and from Nayak et al. (2016) having a resolution of 2″), and results in the LMC (excluding 30 Doradus) from Wong et al. (2011), whose study had a spatial resolution of 45″. Note that the clouds of Pineda et al. (2009) and Nayak et al. (2016) do not cover the central region of 30 Doradus near R136, and there are no spatial overlaps between the KN clouds and the clouds they identify. The molecular clouds associated with the stapler nebula lie above the canonical σ_v–r relation for Galactic clouds. Interestingly, the other clouds detected in 30 Doradus from Pineda et al. (2009) and Nayak et al. (2016) also lie above the canonical relation. Although the departure from the relation is not at the same scale as the KN clouds, this might still indicate that the observed σ_v–r relation might be a function of distance from R136 and a more global property of 30 Doradus.

The position of the KN molecular clouds in the σ_v–r diagram implies one of two scenarios: either the clouds are collapsing or expanding, or the observed line widths are the manifestation of external pressures that keep the clouds in equilibrium. Since collapse velocities are generally only $\sim$40% larger than equilibrium velocity dispersions for a self-gravitating cloud, the observed large line widths for the sizes of the KN clouds are probably not the result of collapse (Ballesteros-Paredes et al. 2011). Neither are they likely to result from expansion because there is no obvious shell or hole structure that usually accompanies expansion.

We examine whether the observed large σ_v are the manifestation of external pressures necessary to keep the clouds in equilibrium. In Figure 4(b), we plot the mass surface density (Σ_{H_2}) against the σ_v^2/r value of the KN clouds, along with results for clouds in the Milky Way from Heyer et al. (2009), in 30 Dor from Pineda et al. (2009) and Nayak et al. (2016), and in the LMC from Wong et al. (2011). Isolated virial clouds confined by self-gravity follow a linear relation in the plot of σ_v^2/r versus Σ_{H_2} (for example, see Heyer et al. 2009). The values for clouds from the literature fall along this expected relation. However, the KN clouds alone depart from it, and are likely confined by external pressure and not in virial equilibrium. Following the simplifying assumptions of Field et al. (2011), we plot isobars of external pressure (in terms of P/k_B) according to their prescription. The lines reflect the external pressure necessary to confine clouds for a given σ_v^2/r, assuming clouds with a centrally concentrated internal density structure approximated by hydrostatic equilibrium. From Figure 4(b), we see that external pressures of $\sim 10^6\ cm^{-3}\ K$ are necessary to keep the KN clouds confined. These values are in general agreement with Chevance et al. (2016), who report that the stapler nebula is located in a region with gas pressure $\sim(0.85-1.2) \times 10^6\ cm^{-3}\ K$, with the peak found in KN2 (see Figure 15 in Chevance et al. 2016).

3.2.2. Variation in Properties as a Function of Distance from R136

The V_{lsr} and M_{H_2} of each cloud are plotted as a function of projected distance from R136 in Figure 5. The velocity of the clouds increases as a function of projected distance from R136.

The velocity of the KN3 cloud loosely matches the radial velocities of the stars within R136.[8] The KN1 cloud is closest in projection to R136 and is blueshifted with respect to the mean velocity of stars in the cluster. This suggests that the KN1 cloud (and likely KN2 and KN3 clouds as suggested by the lack of background stars) lies slightly in front of the cluster. The clouds appear to be moving away from the cluster as a function of projected distance from it (Figure 5(a)).

M_{H_2} of each cloud also increases as the projected distance from R136 increases (Figure 5(b)). The mass of the KN1 cloud is approximately half that of the KN3 cloud. If it is assumed that the molecular clouds detected in CO(2–1) were initially all of similar densities and that photoionization from R136 alone is evaporating the molecular cloud, then KN1 must be closer to R136 (considering it as the only source of external photoionization) because the ionizing flux decreases with the inverse square of distance.

3.3. Line-of-sight Distances

Our main results concerning the detection of cold molecular gas near R136 suffer from possible projection effects. Although the cold molecular gas detected in the CO(2–1) observations lies within 2–14 pc in projection of the R136 cluster, the actual distance may likely be further in the line-of-sight direction, allowing for the clouds to possibly survive photoionization. Chevance et al. (2016) analyze the physical distance of the CO gas in 30 Doradus from the stars, by comparing the radiation field incident on the gas modeled against fIR observations in fine-structure lines of the emitted radiation field measured from the known massive star population. By comparing the luminosity of the photodissociation region (which forms the interface between the photoionizing radiation from the stars and the gas) against their predictions, they are able to constrain the line-of-sight distance of the photodissociation regions from R136 with uncertainties of 4 pc. Based on their results (Figure 20 in Chevance et al. 2016), the stapler nebula lies less than 20 pc away in the line-of-sight direction from R136, which itself lies at the center of a sphere of about 6 pc in radius. This distance agrees well with the line-of-sight distance measured from line ratios of ionized lines in optical spectra by Pellegrini et al. (2010). From their Figure 12, we find that the KN clouds are less than 20 pc away from R136 along our line of sight.

We also consider that if the CO gas is close to R136 and coincident with the dust, there is likely to be a gradient (reflecting the gradient in the projected V_{lsr}) in the dust temperature and in the total fIR luminosity arising from the photodissociation region. Such a gradient is visible both in the maps of dust temperature (Guzman 2010) and in the total fIR luminosity, which peaks at KN2 and decreases toward KN3 (see Figure 1 of Chevance et al. 2016). Therefore, although our observations are unable to resolve the line-of-sight distances to the KN clouds from R136, based on corroboration from multiple independent sources in the literature, we find that the line-of-sight distance to the KN clouds from R136 is ≲20 pc. The molecular clouds in the stapler nebula lie between 2 and 14 pc in projected distance, and ≲20 pc in line-of-sight distance from R136.

4. Near-infrared Emission Line Imaging

The H_2 2.12 μm emission line image is shown in Figure 2(c) with the CO(2–1) contours overlaid. Strong H_2 emission is spatially coincident with the CO(2–1) emission of the molecular clouds and shares similar morphology. The H_2 emission is clumpy, with numerous knots and a reticulated pattern. In contrast, detected ionized gas (Brγ) at the position of the CO(2–1) molecular clouds is weak and diffuse (see Figure 2(d)). This diffuse Brγ emission is associated with filaments and arc-like structures of ionized gas vivid in Hα (brown in Figure 2(a)). This convinces us that the strong H_2 nIR emission is the warmer component of the cold molecular gas traced by the CO detections, whereas the diffuse Brγ emission lies slightly beyond the ionized surface of the molecular cloud although no clear demarcation is noted. The Brγ morphology is not spatially coincident with the H_2 and CO (2–1) emission.

The H_2/Brγ ratio can be used to disentangle shock/collisionally excited H_2 from fluorescence excitation. This is because the shocks and collisional excitation affect primarily the H_2 gas, leaving the ratio of H_2/Brγ above unity, whereas fluorescence acts on both the molecular and ionized gas, leading to a ratio below unity. Using the absolute flux ratio, we find that the H_2/Brγ ratio never exceeds 0.5 at an angular resolution of 1″ in the stapler nebula, agreeing with the findings of Yeh et al. (2015). This indicates that the excited nIR H_2 is primarily excited by the ultraviolet (UV) radiation from R136 acting on the surfaces of the molecular gas, with the filamentary Brγ arising from the same source. The KN clouds therefore must lie in front of us, given the morphology of the clumped H_2 emission and lack of background stars. We note that it is possible that shock-excited emission is prevalent on smaller scales (a few tenths of a parsec, or ≲0″5 at the distance to 30 Doradus) caused by outflows from massive protostars residing within the KN molecular clouds, but our current limitations on angular resolution in the nIR narrowband images (∼1″) prevent us from examining the same in detail. Future integral field unit (IFU) nIR spectroscopy at high angular resolution would help toward constraining this further, because shocked gas will likely be offset in velocity.

A picture of ionization fronts emerges, with the photodissociation region extincted from our line of sight by the cold molecular gas. These structures could resemble the dense "pillars" or structures observed in the Galaxy in regions such as M16 and NGC 3603 (Sankrit & Hester 2000), though they are smaller in scale at ∼0.1–0.3 pc, and also observed in the 30 Doradus nebula by Pellegrini et al. (2010). From the observed emission line imaging and CO(2–1) observations it appears that the clouds are being ionized on the far side. We are viewing the KN molecular clouds face-on, and they are likely the tail of pillar-like structures (we refer the reader to Pound 1998 for a description of pillar morphology, or to Figure 7) with the ionized head pointing toward R136. The observed velocity line widths of the CO(2–1) line are then likely caused by the velocity gradient between the head and tail of pillars (e.g., Pound 1998). Following the analytical theory of photoevaporating clouds due to Bertoldi (1989), during photoevaporation clouds form a cometary structure similar to pillars. Neutral gas at the head is pushed back by the ionization front stripping the outer envelope. The difference in velocity between the slowly moving head and the tail with respect to ionizing stars creates a velocity gradient, which is manifested as the velocity line width
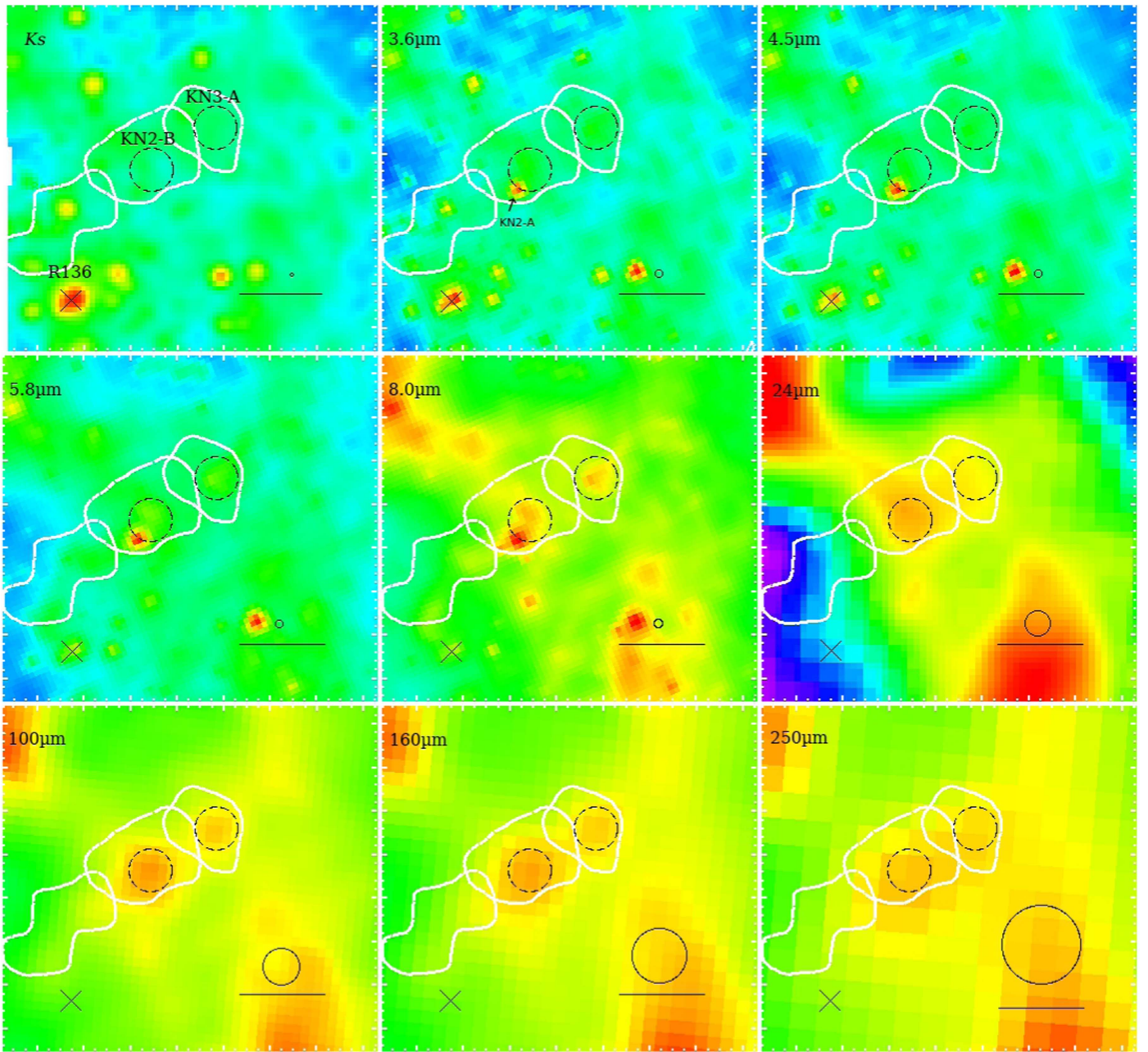

Figure 6. Ks 250 μm inverted color thumbnails with the positions of KN2-B (bottom) and KN3-A (top) overlaid as dashed circles. Scale is linear. Each circle has a radius of 5″, while the cross marks the position of R136. The scale bar in the bottom right corner is of 20″, or ≈5 pc at the distance to the LMC. The FWHM of each image is given by the solid circle above the scale bar. From the images, KN2-B and KN3-A are not visible at short wavelengths but have PAH emission associated with them in the 8 μm image (the PAH feature is at 8.6 μm and falls within the bandwidth). At 24 μm, emission likely arising from protostellar heating of the surroundings is visible at the position of KN2-B but not in KN3-A. At longer wavelengths of 100 and 160 μm from the *Herschel* imaging, both KN2-B and KN3-A are visible as point-like sources. However, at 250 μm, only KN2-B appears significant, with KN3-A extended. Also shown are the outermost contours for each of the KN clouds from Figure 2(a). In the 3.6 μm, the position of KN2-A is given by the arrow. The source is not bright at Ks or wavelengths >10 μm.

Table 2
Candidate Class 0/I YSOs from *Spitzer* and *Herschel* Photometry

ID	Wavelength (μm)	R.A. (J2000)	Decl. (J2000)	Class	α_{SED}	Comments
KN2-A	1.2–8	$05^h38^m39^s7$	$-69°05'38''1$	II	1.22 ± 0.2	S5 in Walborn et al. (2013)
KN2-B	100–350	$05^h38^m39^s1$	$-69°05'33''8$	0	⋯	$T_b = 29 \pm 4$ K; point-like in 24 μm imaging
KN3-A	3.6–500	$05^h38^m36^s3$	$-69°05'24''$	Dust(?)	2.65 ± 0.7	$T_b = 31.5 \pm 7$ K; extended in 24 μm imaging
						0″9 between *Herschel* 100 μm and *Spitzer* sources
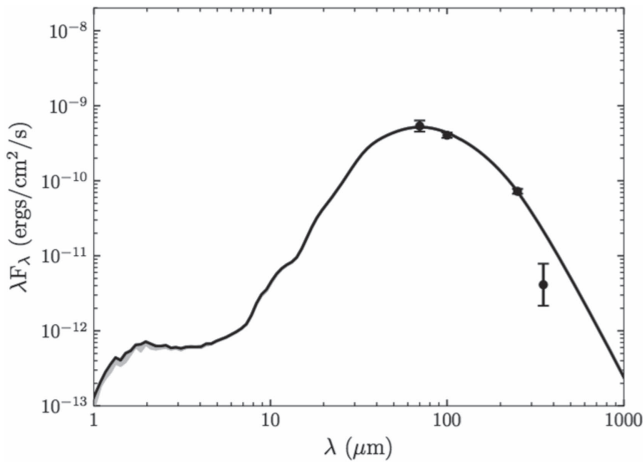
Figure 7. SED of KN2-B with best-fit models from Robitaille (2017), overlaid with *Herschel* 100–350 μm photometry and corresponding error bars. The best-fit model (with χ^2/datapoint<3) with a stellar temperature of ∼18,500 K is shown as a solid black line. Other models with χ^2/datapoint<5 are also shown as solid gray lines.

seen in Figure 4 and also provides a natural explanation for the observed properties of the molecular clouds. The observed velocity line widths are in a similar range to those observed in M16 using CO observations (Pound 1998). Our results are well supported by the work presented in Chevance et al. (2016). The stapler nebula is prominent in forbidden mIR and fIR line emission from [S II], [C II], and [O II] (Figure 1 in Chevance et al. 2016), which are key tracers of photodissociation regions.

5. Candidate Massive YSOs

5.1. Identification of YSOs

Our aim is to detect any on-going star formation through the identification of YSOs using archival infrared photometry. The youngest YSOs (Class 0 objects) will only be visible at $\lambda > 10\,\mu m$, while older Class I/II sources will be visible at shorter (>2 μm) wavelengths. Using *Spitzer* 3.6–24 μm and *Herschel* 100–350 μm photometry (details in Section 2.3, and images are presented in Figure 6), we classify point or point-like sources either based on the slope of the spectral energy distribution (SED) in the 3.6–24 μm wavelength range or by examining the parameters derived from fitting modified blackbody and YSO models across the entire wavelength range. We require detection in at least three bands in each catalog to classify the object as a source. We then check for any counterparts with the coordinates of the detection in the *Herschel* 100 μm within a cross-match radius of 6″.7 (which is the convolution kernel at 100 μm) and the *Spitzer* coordinates. We find a known *Spitzer* source in KN2 (KN2-A, or S5 in Walborn et al. 2013), a *Herschel* source without a *Spitzer* counterpart in KN2 visible at 100–350 μm (KN2-B), and one *Herschel* source with a *Spitzer* counterpart within 0″.9 in KN3 (KN3-A). Thumbnails of these sources in the *Spitzer* and *Herschel* bands are shown in Figure 6.

For SED fitting, we utilize three methods to derive the properties of the source. First, we fit the photometry of each source with the YSO models of Robitaille (2017). The model grid covers 20,000 radiative transfer YSO models covering a mass range of 0.1–50 $M_\odot$. It should be noted that the SED fits are intended not to provide accurate parameters but to serve as a crude guide to the nature of each source, and that these

models are limited in nature compared to the available free parameters (Offner et al. 2012). Second, we use a modified blackbody fit to the fIR *Herschel* sources to constrain the temperature of the emitting source, T_b. The observed flux can be reproduced as a blackbody with frequency flux density F_ν as

$$F_\nu = B_\nu(T_b)(1 - e^{-\tau_\nu})\Omega. \tag{8}$$

Here, $B_\nu(T_b)$ is the blackbody emission at T_b, and τ_ν is the optical depth constrained by a power law at frequency ν by $\tau_\nu \propto \nu^\beta$; $\beta = 1.5$ in the LMC (Galliano et al. 2011). Third, for just the *Spitzer* sources we employ the slope of the SED fit (α_{SED}), where

$$\alpha_{SED} = \frac{d \log(\lambda F_\lambda)}{d \log \lambda}. \tag{9}$$

We consider only the flux in the wavelength range 3.6–24.0 μm, which classifies well Class I/II sources (e.g., Greene et al. 1994). The results of our analysis are presented in Table 2 and described in the following subsections.

5.2. Description of YSOs in the Clouds

5.2.1. KN1 Cloud

KN1 contains no identified mIR or fIR source.

5.2.2. KN2 Cloud

KN2 is extremely promising as a site of future massive star formation. KN2-B is a *Herschel* source detected in 100–350 μm imaging (marked in Figure 6). No near counterpart mIR source exists. The nearest mIR source is KN2-A, which lies to its immediate southwest and at the very edge of the CO emission. This source angularly coincides with the dense region observed in CS to the south of KN2 by Rubio et al. (2009). CS is a tracer of dense gas with densities n upwards of $10^5\,cm^{-3}$.

KN2-B is classified as a high-mass YSO based on the *Herschel* classification scheme devised by Seale et al. (2014) for YSOs in the Magellanic Clouds. Following their three classification criteria (see Section 4.4 of that paper for further details), we find that KN2-B meets all three because it is (i) the dominant source of fIR photometry and is clearly defined in at least three *Herschel* bands at 3σ above the background, (ii) it is not identified as a background galaxy/interloper, and (iii) it has 24 μm emission as seen in Figure 6. The source has marked polycyclic aromatic hydrocarbon (PAH) emission from the 8.6 μm feature.

We achieve an excellent fit for KN2-B with the SED models of Robitaille (2017). The best fit has χ^2/data point <3 and is shown in Figure 7. The parameters of the best-fit model were a stellar temperature of $18{,}500 \pm 1000$ K, which translates to a stellar mass exceeding 20 $M_\odot$, with $\dot{M}_{env}/M_*$ from the model fit suggestive of a Class 0 massive YSO (Figure 7). The temperature estimated from the blackbody fit is 28.8 ± 4 K, with the integrated logarithm of luminosity $\log L/L_\odot = 4.59$, which further indicates a Class 0 classification (André et al. 2010). The luminosity of the source is much higher than expected for starless clouds heated by the nascent radiation field; in view of this it is likely a true high-mass YSO (Seale et al. 2014). The estimated extinction from the SED fit (of $A_V = 6.9$) suggests that the candidate protostar is shielded from external photoionization. Moreover, the external heating at wavelengths longwards of 100 μm does not significantly
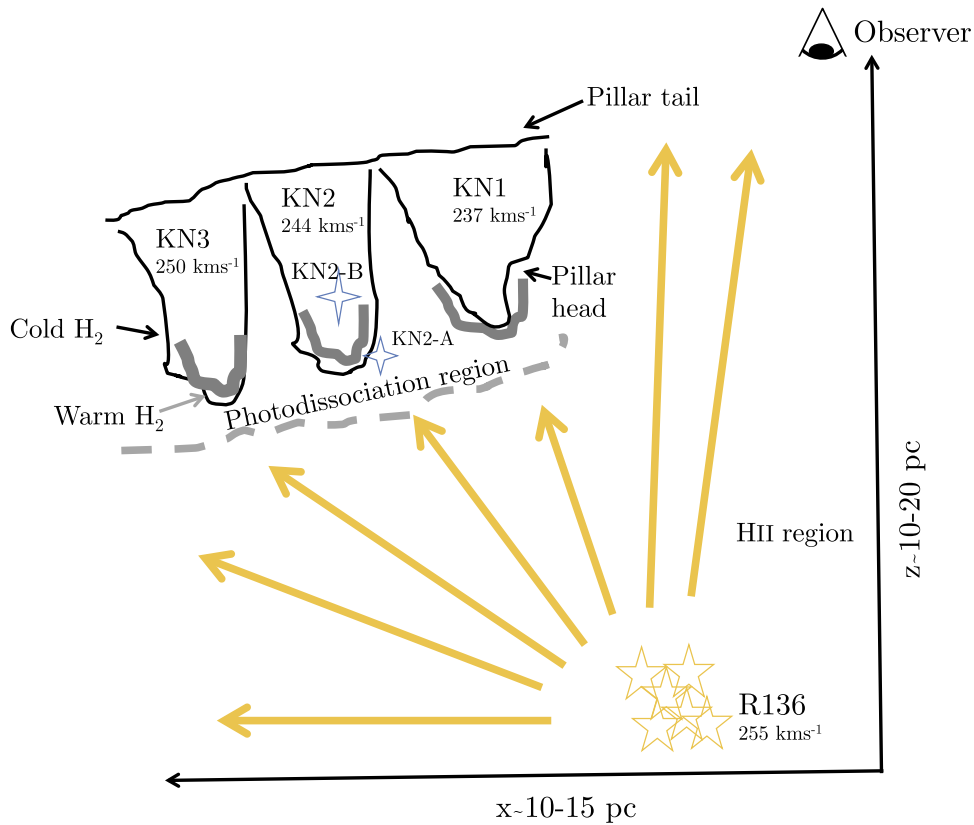
Figure 8. Schematic of the stapler nebula. The model is flattened in the *y* direction, with the direction of the observer on the *z*-axis indicated. Ionizing radiation from the massive R136 stars (yellow symbols, with the mean radial velocity given in the frame of the local standard of rest) photoionizes (indicated by yellow arrows) the blueshifted cold molecular gas lying in pillar-like features (solid lines), leading to the observed CO(2–1) line widths. This leads to a photoionization region in the head of the pillar from where the Brγ emission arises (gray thick lines). The tail of the pillar is comparatively colder, and is where the cold molecular gas is detected. The individual molecular clouds are identified along with their central velocities in the frame of the local standard of rest. In KN2, we detect the candidate protostar KN2-B (indicated by the large blue star), which is likely a forming high-mass star. The previously known YSO candidate KN2-A is also shown as a small blue star.

affect the SED (Pavlyuchenkov et al. 2012). Finally, as noted in Section 5.1, the parameters estimated from the SED fits with the models of Robitaille (2017) may be ambiguous due to the limited range of parameters considered, but they do provide a crude guide to source classification. We also stress that KN2-B is classified as a high-mass YSO based on the independent schemas of Seale et al. (2014), which are based on source intensity and morphology, and the SED models of Robitaille (2017), which are based on the flux distribution of the source in the fIR. The age of KN2-B from the model fit is $\lesssim 0.1$ Myr, which is smaller by an order of magnitude than the crossing timescale of the cloud of 0.66 Myr (the crossing timescale is the length divided by the velocity).

KN2-A is likely a Class II source based on its *Spitzer* colors. The α_{SED} slope derived from the 3.6–8 μm photometry is 1.22 ± 0.2, which falls into the Class II category (Greene et al. 1994). Our classification as a Class II YSO from the SED slope agrees with the classification of Gruendl & Chu (2009) based on the position of KN2-A in *Spitzer* color–color and color–magnitude diagrams. We note that there is no 24 μm counterpart to KN2-A, and it also does not have a *Herschel* counterpart as a result of the cross-matching procedure followed by Seale et al. (2014), who cross-match *Spitzer* and *Herschel* catalogs in the LMC. They adopt a cross-match radius of 0.5 × FWHM to cross-match the two catalogs in crowded regions. If we still consider that some of the fIR flux from KN2-A is assigned to KN2-B, we find that $\gtrsim 5\%$ of the fIR flux of KN2-B is required to change the classification of KN2-A

from Class II to Class I. There is no population of high-mass Class II YSOs on the northern side.

5.2.3. KN3 Cloud

KN3-A is a bright *Herschel* source and is extended in 100–350 μm imaging. The *Herschel* detection lies within 0″.9 of a *Spitzer* source found by Gruendl & Chu (2009). We consider the mIR and fIR detections to be of the same source, because they lie well within the FWHM of the *Herschel* and *Spitzer* imaging. Gruendl & Chu (2009) classified the source as likely originating from dust, and we see that there exists no point-like or otherwise 24 μm counterpart. The whole SED fits rather poorly with the models of Robitaille (2017), with the best fits achieved when discarding the 4.5 μm photometry of χ^2/data point >100. Examination of the 24 μm imaging reveals no distinct point-like source (Figure 6; right dashed circle). Given the flux at long wavelengths, and the extended visible emission in the imaging, we cannot classify the source as a YSO conclusively. A modified blackbody fit suggests a peak temperature of 31.5 ± 6 K, with the integrated total luminosity slightly less than $10^4 L_\odot$. This lies at the boundary of the classification scheme between interstellar starless clouds heated by the nascent radiation field (Seale et al. 2014) and YSOs. The ambiguous classification and the lack of any clear point-like source in the nIR and fIR images suggest that this source is likely a starless dust cloud, probably heated by the nascent ionizing field.

A comparison of the multi-wavelength images in Figure 6 demonstrates the differences between KN2-B and KN3-A. At 24 μm, diffuse emission in star-forming regions is likely to originate from heated gas from the inner regions of protostars (Chambers et al. 2009). In KN2-B, the 24 μm emission is clearly detected at the 3σ level with respect to the immediate surroundings. In KN3-A, no 24 μm emission is detected above the 3σ threshold. At 100 μm and 160 μm, both sources appear as point sources. But, at longer wavelengths, the KN3-A source is extended or disappears (see the 250 μm image), suggesting that it is more likely to be dust rather than a protostellar candidate when compared to the nature of the source detected at the position of KN2-B in the 250 μm image.

6. A Picture of the Stapler Nebula in R136

From our deep CO(2–1) observations, we identified three molecular clouds separated in velocity that we name KN1–KN3 lying within 14 pc in projection and $\lesssim$20 pc in the line of sight from the YMC R136. These clouds lie north of R136 and stretch for 14 pc in projection from southeast to northwest. This axis is perpendicular to the giant molecular clouds previously identified by Johansson et al. (1998). V_{lsr} of the clouds ranges from 237 km s^{-1} for the cloud directly above R136 in projection to 250 km s^{-1} for the furthest cloud, which is similar to the mean radial velocity of the stellar population in R136. These clouds display relatively large line widths for their radii, lying above the predicted relation for clouds in virial equilibrium according to Larson's first law. By plotting σ_v^2/r of the KN clouds as a function of their Σ_{H_2}, we show that KN clouds depart significantly from the relation for virialized, isolated clouds confined by self-gravity. The KN clouds are most likely confined by external pressures upwards of $\sim 10^6$ cm^{-3} K in this scenario. Nonetheless, the results from our CO(2–1) line observations show that there are three molecular clouds lying near R136, whose V_{lsr} increases as a function of projected distance from the cluster. The resolved clouds are not in virial equilibrium but are highly turbulent, requiring external pressure to confine them.

Brγ and H$_2$ nIR emission line imaging reveals that the CO clouds coincide with the dense H$_2$ clumpy structures, while Brγ is diffuse and exhibits little spatial coincidence with the CO clouds. The lack of background stars at optical wavelengths (Figure 1) suggests that these clouds lie in front of the cluster. Based on the H$_2$/Brγ ratio, we suggest that these clouds are UV-heated by stellar radiation emanating from R136. These results suggests that both the H$_2$ nIR emission and CO emission arise from molecular clouds near R136. The molecular clouds lie in front of R136 from our perspective. The far side of the molecular clouds is being ionized by R136, leading to diffuse Brγ emission and weak Hα emission. The excited H$_2$ emission coincides with the peak of CO emission, further giving weight to our view of photodissociated molecular clouds near R136.

Finally, a search for results of on-going star formation yields interesting results. KN1 shows no signs of active star formation. In fIR *Herschel* 100–350 μm photometry, we identify a likely Class 0/I object KN2-A corresponding to the peak of the molecular cloud KN2. It is known from previous CS observations that the densities near this source are $n > 10^6$ cm^{-3}. Near this source (within 5″) lies a Class II object KN2-A visible in *Spitzer* imaging, which has been classified as a YSO by Gruendl & Chu (2009) and Walborn et al. (2013). Toward KN3, we detect a 100–160 μm source

(KN3-A) close to a *Spitzer* source identified by Gruendl & Chu (2009). However, inspection of both the *Spitzer* and *Herschel* imaging suggests that KN3-A is likely dusty in nature, which agrees with the classification of Gruendl & Chu (2009).

The complete scenario can be visualized in the toy model shown in Figure 8 along with the observer's viewpoint. The natal molecular cloud of R136 has an arc-like structure, protruding in front of it along our line of sight, and lying directly above it and stretching toward the northwest in projection. The structure may have been carved out from an initially spherical cloud. After the formation of the cluster, the natal molecular cloud has been steadily ionized, giving rise to excited H$_2$ emission. The excited boundary lies on the far side of the molecular cloud from the observer's viewpoint. The radiation from R136 is eroding the molecular clouds, possibly leading to the formation of structures similar to the "pillars of creation" observed in Galactic regions such as M16. The observer may be seeing the tail of such pillars face-on. The observed high velocity line widths could then be explained as a manifestation of the expected velocity differences between the head and tail of a photoevaporating cloud. Alternatively, the results also support the picture that the KN clouds may likely be confined by external pressures. IFU spectroscopy of the clouds at high angular resolution, which will reveal their gas kinematics and ionization structure (McLeod et al. 2015), can help differentiate between the two proposed scenarios. Massive star formation is occurring in the middle molecular cloud or pillar, while the other two clouds show no active signs of massive star formation.

7. Summary and Future Work

Our results present a picture of three CO molecular clouds separated in velocity, lying $\lesssim$20 pc in front of R136 and between 2 and 14 pc away in projection from the cluster. We appear to view the tail of pillar-like structures whose ionized heads are pointing toward R136. The observed large line widths of the molecular clouds for their sizes with respect to the canonical σ_v–r relation are likely due to the gas being pushed away from the head of the pillar-like structures by the ionizing radiation produced by the massive stars in R136, or due to external pressure confining the clouds. A massive YSO (KN2-B) is detected inside the KN2 molecular cloud, indicating active star formation. These results suggest that the 1.5–3 Myr old cluster R136 is in the process eroding the KN molecular clouds. During this process a new generation of stars is able to form from the reservoir of cold molecular gas that is in the process of being destroyed by stellar feedback in structures that may be similar to the pillars of creation seen in Galactic regions such as M16 and NGC 3603 from a different perspective.

We have demonstrated that with sensitive CO(2–1) observations, molecular clouds of $\sim 10^4 M_\odot$ exist surprisingly close to the YMC R136. This observation challenges the results of most simulations of feedback from massive stars in YMCs (see Dale 2015 for a review), where feedback is able to successfully expel gas close to YMCs within a few million years. Future sensitive observations of multiple molecular lines at high angular resolution using the current generation of interferometers (e.g., using the Atacama Large Millimeter/submillimeter Array (ALMA), which can achieve a resolution comparable to optical/nIR imaging in CO lines) may reveal in exquisite detail the structure and densities of these clouds. Combined with observations of the photodissociation region from fine-structure

lines (Chevance et al. 2016), one can gather enough information about the densities, pressures, and radiation field acting on the KN clouds and the H II region to predict whether the clouds are dense and massive enough to survive photoionization and form a new massive stellar cluster, or whether star formation will be abruptly terminated due to feedback. In a broader sense, sensitive radio observations in CO lines may reveal previously undetected molecular clouds lying close to YMCs, which may nurture a new generation of star formation.

ORCID iDs

Venu M. Kalari ⬤ https://orcid.org/0000-0002-4641-2532
Bruce G. Elmegreen ⬤ https://orcid.org/0000-0002-1723-6330

References

Anderson, C. N., Meier, D. S., Ott, J., et al. 2014, ApJ, 793, 37
André, P., Men'shchikov, A., Bontemps, S., et al. 2010, A&A, 518, L102
Ballesteros-Paredes, J., Hartmann, L. W., Vázquez-Semadeni, E., Heitsch, F., & Zamora-Avilés, M. 2011, MNRAS, 411, 65
Bertoldi, F. 1989, ApJ, 346, 735
Bolatto, A. D., Leroy, A. K., Rosolowsky, E., Walter, F., & Blitz, L. 2008, ApJ, 686, 948
Bolatto, A. D., Wolfire, M., & Leroy, A. K. 2013, ARA&A, 51, 207
Brandner, W., Grebel, E. K., Barbá, R. H., Walborn, N. R., & Moneti, A. 2001, AJ, 122, 858
Chambers, E. T., Jackson, J. M., Rathborne, J. M., & Simon, R. 2009, ApJS, 181, 360
Chevance, M., Madden, S. C., Lebouteiller, V., et al. 2016, A&A, 590, A36
Cutri, R. M., Skrutskie, M. F., van Dyk, S., et al. 2003, yCat, 2246, 0
Dale, J. E. 2015, NewAR, 68, 1
Dale, J. E., Ercolano, B., & Bonnell, I. A. 2012, MNRAS, 427, 2852
De Marchi, G., Panagia, N., Romaniello, M., et al. 2011, ApJ, 740, 11
Evans, C. J., Kennedy, M. B., Dufton, P. L., et al. 2015, A&A, 574, A13
Field, G. B., Blackman, E. G., & Keto, E. R. 2011, MNRAS, 416, 710
Galliano, F., Hony, S., Bernard, J.-P., et al. 2011, A&A, 536, A88
Greene, T. P., Wilking, B. A., Andre, P., Young, E. T., & Lada, C. J. 1994, ApJ, 434, 614
Gruendl, R. A., & Chu, Y.-H. 2009, ApJS, 184, 172
Guzman, V. V. 2010, MSc thesis, Universidad de Chile
Herrera, C. N., Rubio, M., Bolatto, A. D., et al. 2013, A&A, 554, A91
Heyer, M., Krawczyk, C., Duval, J., & Jackson, J. M. 2009, ApJ, 699, 1092
Indebetouw, R., Brogan, C., Chen, C.-H. R., et al. 2013, ApJ, 774, 73
Johansson, L. E. B., Greve, A., Booth, R. S., et al. 1998, A&A, 331, 857
Kalari, V. M., Vink, J. S., Dufton, P. L., et al. 2014, A&A, 564, L7
Larson, R. B. 1981, MNRAS, 194, 809
Lombardi, M., Alves, J., & Lada, C. J. 2010, A&A, 519, L7
MacLaren, I., Richardson, K. M., & Wolfendale, A. W. 1988, ApJ, 333, 821
Maloney, P. 1988, ApJ, 334, 761
McKee, C. F., & Ostriker, E. C. 2007, ARA&A, 45, 565
McLeod, A. F., Dale, J. E., Ginsburg, A., et al. 2015, MNRAS, 450, 1057
Meixner, M., Gordon, K. D., Indebetouw, R., et al. 2006, AJ, 132, 2268
Meixner, M., Panuzzo, P., Roman-Duval, J., et al. 2013, AJ, 146, 62
Nayak, O., Meixner, M., Indebetouw, R., et al. 2016, ApJ, 831, 32
Offner, S. S. R., Robitaille, T. P., Hansen, C. E., McKee, C. F., & Klein, R. I. 2012, ApJ, 753, 98
Pavlyuchenkov, Y. N., Wiebe, D. S., Akimkin, V. V., Khramtsova, M. S., & Henning, T. 2012, MNRAS, 421, 2430
Pellegrini, E. W., Baldwin, J. A., & Ferland, G. J. 2010, ApJS, 191, 160
Persson, S. E., Murphy, D. C., Krzeminski, W., Roth, M., & Rieke, M. J. 1998, AJ, 116, 2475
Pietrzyński, G., Graczyk, D., Gieren, W., et al. 2013, Natur, 495, 76
Pineda, J. L., Ott, J., Klein, U., et al. 2009, ApJ, 703, 736
Pound, M. W. 1998, ApJL, 493, L113
Robitaille, T. P. 2017, A&A, 600, A11
Rolleston, W. R. J., Trundle, C., & Dufton, P. L. 2002, A&A, 396, 53
Roman-Duval, J., Gordon, K. D., Meixner, M., et al. 2014, ApJ, 797, 86
Rubio, M., Barbá, R. H., Walborn, N. R., et al. 1998, AJ, 116, 1708
Rubio, M., Paron, S., & Dubner, G. 2009, A&A, 505, 177
Sankrit, R., & Hester, J. J. 2000, ApJ, 535, 847
Schneider, F. R. N., Sana, H., Evans, C. J., et al. 2018, Sci, in press
Seale, J. P., Meixner, M., Sewiło, M., et al. 2014, AJ, 148, 124
Selman, F. J., & Melnick, J. 2013, A&A, 552, A94
Solomon, P. M., Rivolo, A. R., Barrett, J., & Yahil, A. 1987, ApJ, 319, 730
Walborn, N. R., Barbá, R. H., & Sewiło, M. M. 2013, AJ, 145, 98
Walborn, N. R., Maíz-Apellániz, J., & Barbá, R. H. 2002, AJ, 124, 1601
Whitney, B. A., Sewilo, M., Indebetouw, R., et al. 2008, AJ, 136, 18
Wong, T., Hughes, A., Ott, J., et al. 2011, ApJS, 197, 16
Yeh, S. C. C., Seaquist, E. R., Matzner, C. D., & Pellegrini, E. W. 2015, ApJ, 807, 117